



2000 PPI silicon-based AlGaInP red micro-LED arrays fabricated via wafer bonding and epilayer lift-off

YONGZHOU ZHAO,^{1,2} JINGQIU LIANG,¹ QINGHUI ZENG,³ YANG LI,^{1,2}  PANYUAN LI,^{1,2} KAILI FAN,^{1,2} WENCHAO SUN,^{1,2} JINGUANG LV,¹ YUXIN QIN,¹ QIANG WANG,¹ JIN TAO,^{1,4} AND WEIBIAO WANG^{1,5}

¹State Key Laboratory of Applied Optics, Changchun Institute of Optics, Fine Mechanics and Physics, Chinese Academy of Sciences, Changchun, Jilin 130033, China

²University of Chinese Academy of Sciences, Beijing 100049, China

³State Key Laboratory of Luminescence and Applications, Changchun Institute of Optics, Fine Mechanics and Physics, Chinese Academy of Sciences, Changchun, Jilin 130033, China

⁴taojin@ciomp.ac.cn

⁵wangwb@ciomp.ac.cn

Abstract: In this article, 2000 PPI red silicon-based AlGaInP micro-LED arrays were fabricated and investigated. The AlGaInP epilayer was transferred onto the silicon substrate via the In-Ag bonding technique and an epilayer lift-off process. The silicon substrate with a high thermal conductivity could provide satisfactory heat dissipation, leading to micro-LED arrays that had a stable emission spectrum with increasing current density from 20 to 420 A/cm² along with a red-shift of the peak position from 624.69 to 627.12 nm ($\Delta\lambda = 2.43$ nm). Additionally, increasing the injection current density had little effect on the CIE (x, y) of the micro-LED arrays. Further, the I-V characteristics and light output power of micro-LED arrays with different pixel sizes demonstrated that the AlGaInP red micro-LED array on a silicon substrate had excellent electrical stability and optical output.

© 2021 Optical Society of America under the terms of the [OSA Open Access Publishing Agreement](#)

1. Introduction

Micro-LEDs have attracted increasing research and commercial attention for applications such as micro-displays [1–4], visible light communications [5–11], and optogenetics [12–15] because of their unique advantages, including a high resolution, low power consumption, and high brightness [16–20]. For micro-display applications, numerous blue and green micro-display devices based on III-nitrides already exist [21–25], demonstrating the high potential of micro-LEDs in micro-displays, especially for virtual reality and augmented reality applications.

Red micro-LEDs, as an indispensable component of full-color micro-LED displays, have also become a topic of intense research interest in recent years [26–29]. High-quality red LEDs are mainly based on AlGaInP; they are generally grown on precisely lattice-matched GaAs substrates via metal organic chemical vapor deposition (MOCVD), which can avoid the generation of excess dislocations and realize internal quantum efficiencies >90% [30,31]. However, the GaAs substrate strongly absorbs red light, thus, limiting the light extraction efficiency of the AlGaInP red LED [32–34]. Additionally, the GaAs substrate has poor heat dissipation, which also limits the performance of the AlGaInP red LED. Various studies have been performed to fabricate high-power thin-film LEDs without the GaAs substrate for high brightness. Dawson et al. [35] used PDMS stamps to transfer the AlGaInP epilayer to diamond and glass substrates and obtained stable micro-LED devices. Hrong et al. [28,36] demonstrated that AlGaInP LEDs on metal substrates, such as copper and copper-invar-copper (CIC), have excellent optical, electrical, and

heat dissipation properties. Horng et al. [37] used glue to bond AlGaInP to a sapphire substrate, and then fabricated flip-chip red micro-LEDs after removing the GaAs substrate. However, the following issues exist with the above methods: the PDMS stamp transfer method has a low accuracy and yield when a large number of pixels need to be transferred; the use of Cu or CIC metal substrates result in increased laser scribing difficulty; and the thermal conductivity of a sapphire substrate is as poor as that of a GaAs substrate.

As a commonly used semiconductor material, silicon has mature cutting and thinning processes, and the thermal conductivity of a silicon substrate is 135 W/m·K—which is greater than that of GaAs at 33 W/m·K [33];—which may help reduce the junction temperature of the LED and improve its photoelectric performance. Therefore, in this work, we proposed transferring the AlGaInP epilayer to a silicon substrate via In-Ag thermo-compression bonding to fabricate AlGaInP red micro-LED arrays on silicon substrates. To improve the light output power, we also used an Ag-based reflector, and a metal barrier layer of Cr/Pt to prevent the bonding metal from spreading to the Ag-based reflector, which would have resulted in reduced reflectivity [38–42]. The 2000 PPI silicon-based red micro-LED arrays were obtained using a fabrication process that included wafer bonding, GaAs substrate etching, pixels isolation, trench filling, and electrode fabrication.

2. Experiments

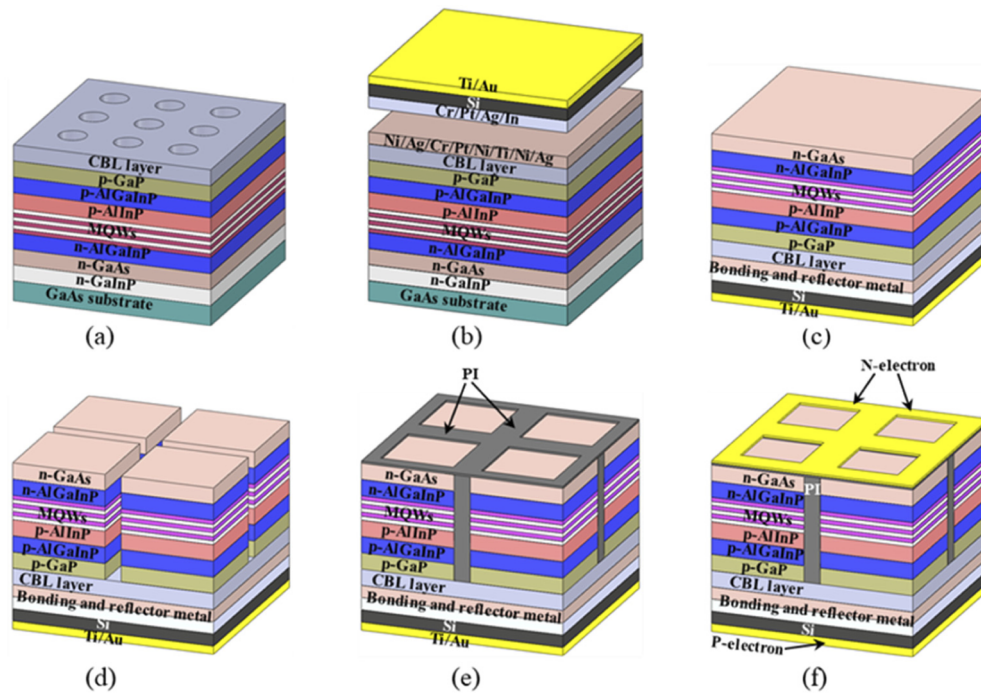


Fig. 1. Schematic illustration of the fabrication process for silicon-based AlGaInP Micro-LED arrays: (a) defining the SiO₂ CBL; (b) deposition of the metallization scheme and bonding to a 4-inch Si wafer; (c) silicon-based AlGaInP epilayer after removing the GaAs substrate and GaInP layer; (d) isolation grooves were etched via an inductively coupled plasma (ICP) etching system; (e) isolation grooves were filled by patterned polyimide (PI); and (f) the AuGeNi/Ag metal electrode was deposited onto n-GaAs layer.

The 4-inch AlGaInP-based LED epilayer was grown on 350 μm GaAs substrates via metalorganic chemical vapor deposition (MOCVD). The LED epitaxial structure consists of a 170 nm-thick n-type GaInP etching stop layer, 80 nm-thick n-type GaAs, 2.3 μm -thick n-type AlGaInP, 350 nm-thick GaInP-AlGaInP MQWs, 300 nm-thick p-type AlInP, 50 nm-thick p-type AlGaInP, and 1.5 μm -thick p-type GaP.

A 300 nm SiO_2 current barrier layer (CBL) was prepared on an epilayer wafer after the LED epilayer was grown, and the holes were etched by reactive ion beam etching (RIE) for electrical connection (Fig. 1(a)). The position of holes and N-electrode was misaligned to increase the later expansion of current. And, Ni/Ag (1 nm/250 nm) was evaporated as the Ag-based reflector layer, Cr/Pt (60 nm/50 nm) was prepared as a bonding metal barrier layer to prevent the bonding metal from spreading to the Ag-based reflector layer, and Ni/Ti/Ni/Ag (20 nm/400 nm/400 nm/2 μm) was evaporated as the bonding metal. Then, Ti/Au (10 nm/100 nm) was prepared on the back of a 4-inch silicon wafer, and Cr/Pt/Ag/In (60 nm/50 nm/1 μm /2 μm) was evaporated on the front of the silicon wafer as the bonding metal layer. Next, the 4-inch LED wafer was bonded to the Si-wafer via thermo-compression bonding at 230°C under 3000 mbar pressure for 30 min. After wafer bonding, the GaAs substrate was removed to expose the GaInP layer using the wet etchant $\text{NH}_4\text{OH}:\text{H}_2\text{O}_2$. Then, the GaInP layer was removed using an HCl solution, followed by annealing under nitrogen protection at 200°C for 15 min to eliminate stress generated by the bonding process. Then, the mesa structures and isolated grooves were formed via inductively coupled plasma (ICP) etching, and the isolated grooves were filled with polyimide (PI). Finally, AuGeNi/Ag (100 nm/1.9 μm) was deposited onto the n-GaAs surface as an n-type ohmic contact followed by rapid thermal annealing in a N_2 atmosphere at 320°C.

3. Results and discussion

The cross-sectional view of the bonding layer between silicon and p-GaP was obtained via SEM, as shown in Fig. 2(a). The cross-section of the bonding layer exhibited a dense structure with no voids, indicating that the In-Ag bonding process had high reliability for bonding the AlGaInP epilayer and silicon wafer.

To analyze the effect of the Ag-based reflector layer, a Ni/Ag layer with the same thickness was deposited on a glass plate, and >90% reflectance was obtained in the red spectral region (seen in Fig. S2(a)). Hence, it is clearly beneficial to use an Ag-based reflector layer to increase the light extraction efficiency. Next, the energy-dispersive X-ray spectroscopy (EDS) of the bonding cross-section was obtained, as shown in Fig. 2(c); it can be seen from the figure that in addition to the bonding metals Pt, Ti, Ag, Cr, and In, we also observed Si from the silicon wafer and Ga and Al from the epilayer. From Fig. 2(b), it can be seen that the surface morphology of the sample after removing the GaAs substrate and GaInP layer is flat. A representative $5 \times 5 \mu\text{m}^2$ AFM micrograph of the sample surface is shown in Fig. 2(d); the root mean square (RMS) of the sample surface was determined to be 5.46 nm, which indicates that the surface of the sample is smooth after lifting off the GaAs substrate and the GaInP layer.

After transferring the AlGaInP epilayer to the silicon substrate and lifting-off of the GaAs substrate and GaInP layer, stress would be generated during the thermo-compression bonding process because AlGaInP and silicon have different thermal expansion coefficients (TECs) (TEC of silicon is $2.6 \times 10^{-6}/\text{K}$ and TEC of AlGaInP is $5 \times 10^{-6}/\text{K}$ [25]). We annealed the epilayer at 200°C for 15 minutes to release stress generated during the wafer bonding process. Next, an ICP etching step was used to selectively etch the sample to realize optical and electrical isolation of each pixel; based on the thickness of the epilayer, the etching depth should be 4.5 μm . Selective ICP etching of the epilayer was then carried out; for this, 650 nm SiO_2 was used as the etching mask and etching was carried out in a mixture of Cl_2 (15 sccm) and N_2 (15 sccm) at 25°C, with 5 mtorr reactor pressure, 600 W ICP power, and 100 W RF power. The measured etch rates reached 580 and 64 nm/min for the epilayer and SiO_2 , respectively. After 465 s of etching time,

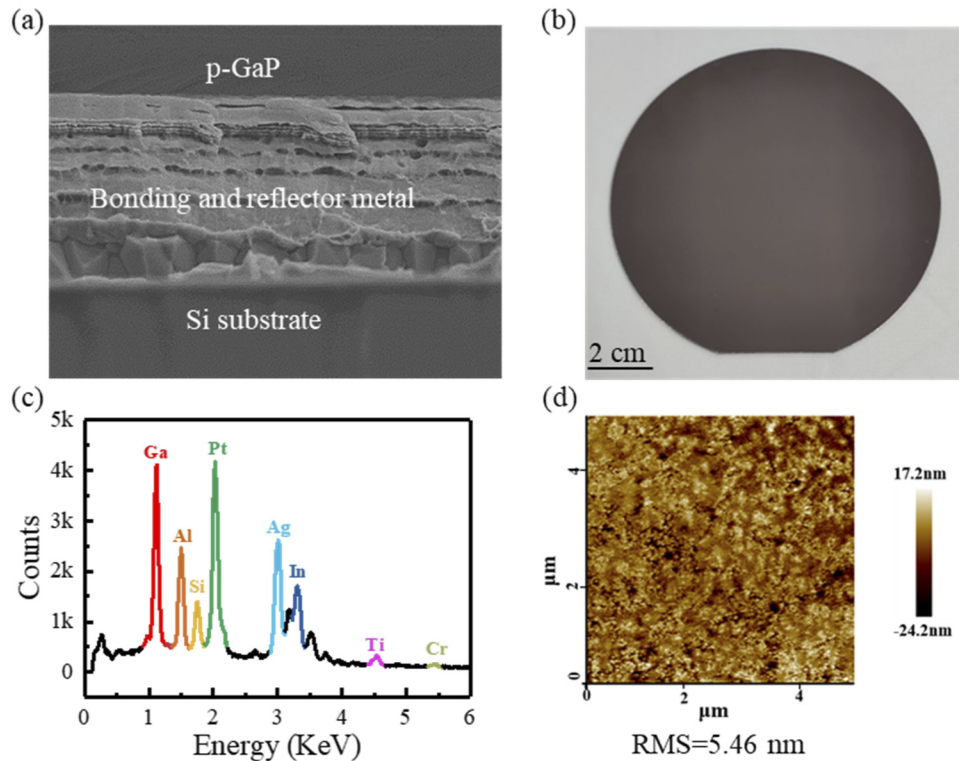


Fig. 2. (a) Cross-sectional SEM image of In-Ag bonding. (b) Side view of the AlGaInP transferred to the silicon substrate. (c) Elemental analysis spectrum of the In-Ag bonding cross-section. (d) Representative $5 \times 5 \mu\text{m}^2$ AFM micrograph of the sample after lift-off the GaAs substrate and GaInP layer.

the etching depth of the micro-LED array with pixel size of $64 \mu\text{m}$ was measured using a surface profiler, as shown in Fig. S2(b). The average etching depth was determined to be $4.5 \mu\text{m}$, as expected. Subsequently, the remaining SiO_2 hard mask was etched via BOE solution.

After ICP etching, the morphology of the micro-LED arrays with different pixel sizes was observed via SEM. The top view image of the isolated grooves and the 2000 PPI micro-LED array with a pixel size of $8 \mu\text{m}$ and pitch of $12 \mu\text{m}$ are shown in Fig. 3(a). Magnified images of one micro-LED and one corner are shown in Fig. 3(b) and Fig. 3(c), respectively. From these SEM images, it can be seen that the low-damage ICP etching recipe results in micro-LEDs with smooth sidewalls.

Then, patterned polyimide (ZKPI-5510M, Beijing Bomi) was used to fill the isolation trench, and AuGeNi/Ag was prepared as the N-electrode to complete fabrication of the micro-LED arrays. To study the difference in the electrical and light output characteristics of different pixel size arrays, we fabricated three types of micro-LED arrays with pixel sizes of 16, 32, and $64 \mu\text{m}$, forming arrays with 8 rows and 8 columns of pixels. They are termed as the $16 \mu\text{m}$ micro-LED array, $32 \mu\text{m}$ micro-LED array, and $64 \mu\text{m}$ micro-LED array, respectively, as shown in Figs. 3(d)–3(f). In addition, the specific contact resistance of AuGeNi/Ag films deposited on the n-GaAs layer via the circular transfer length method (CTLM) was measured. The I-V characteristics were measured for AuGeNi/Ag contacts with different CTLM spacings after annealing at 320°C , as shown in Fig. S2(c). The specific contact resistances were determined from the plots of the measured resistances versus the spacing between the CTLM. The least-square method was used

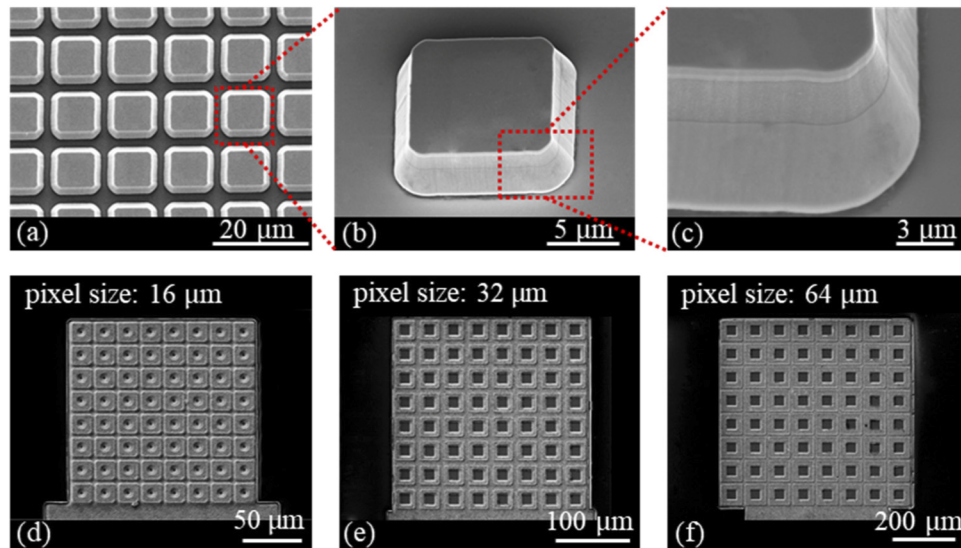


Fig. 3. SEM images of micro-LED arrays with different sizes and pitches. (a) Top-view SEM image of the isolated grooves and a micro-LED array with a pixel size of 8 μm and pitch of 12 μm . (b) Magnified image of a single micro-LED with a pixel size of 8 μm . (c) Magnified image of one corner of a micro-LED with a pixel size of 8 μm . (d) A 16 μm micro-LED array after fabrication. (e) A 32 μm micro-LED array after fabrication. (f) A 64 μm micro-LED array after fabrication.

to fit a straight line to the experimental data, as shown in Fig. S2(d). Here, the measured specific contact resistances of AuGeNi/Ag were $7.48 \times 10^{-3} \Omega \cdot \text{cm}^2$.

The light uniformity of micro-LED arrays with different pixel sizes are illustrated via electroluminescence (EL) images. From Fig. 4, it can be seen that all the micro-LED arrays realized high-resolution display characteristics. The uniformity of the arrays mainly derives from the influence of lithography accuracy and equipment conditions. Particularly, smaller size micro-LED arrays would suffer more non-uniformity. Figure 4(a) shows a 30×30 micro-LED array with a pixel size of 8 μm and a pitch size of 12 μm ; this array has a pixel density >2000 PPI. Figure 4(b) shows a micro-LED array with a pixel size of 16 μm , and a symmetrical pattern is displayed on the array by fabricating only the N-electrons above the lighted pixels. Figure 4(c) is a micro-LED array with a pixel size of 64 μm , and the words ‘CAS’ are displayed in the array by fabricating only the N-electrons above the lighted pixels. In addition, EL images of the three Micro-LED arrays were also captured. Figure 4(d) is a 16 μm micro-LED array, Fig. 4(e) is a 32 μm micro-LED array, and Fig. 4(f) is a 64 μm micro-LED array.

Figure 5(a) shows the EL spectra of the whole micro-LED array with a pixel size of 8 μm at different injection current densities. It is clear that the peak values of the EL spectrum of the micro-LED array increased alongside increasing injection current densities from 40 to 420 A/cm^2 . Additionally, the peak wavelength and full width at half maximum (FWHM) changed slightly with varying current density, which can be attribute to heating of the arrays [36]. Figure 5(b) shows the peak wavelength and FWHM as a function of the injection current density. The peak position redshifts from 624.69 nm to 627.12 nm ($\Delta\lambda = 2.43$ nm) as bias current density varied from 20 to 420 A/cm^2 . The observed performance is better than that of AlGaInP thin-film LEDs on CIC substrates. Horng et al. [28] reported AlGaInP devices on CIC substrates with a peak wavelength change $\Delta\lambda \sim 17$ nm from 20 to 100 A/cm^2 . We also measured the change in peak wavelength of AlGaInP micro-LED on GaAs substrate, and the results were shown in

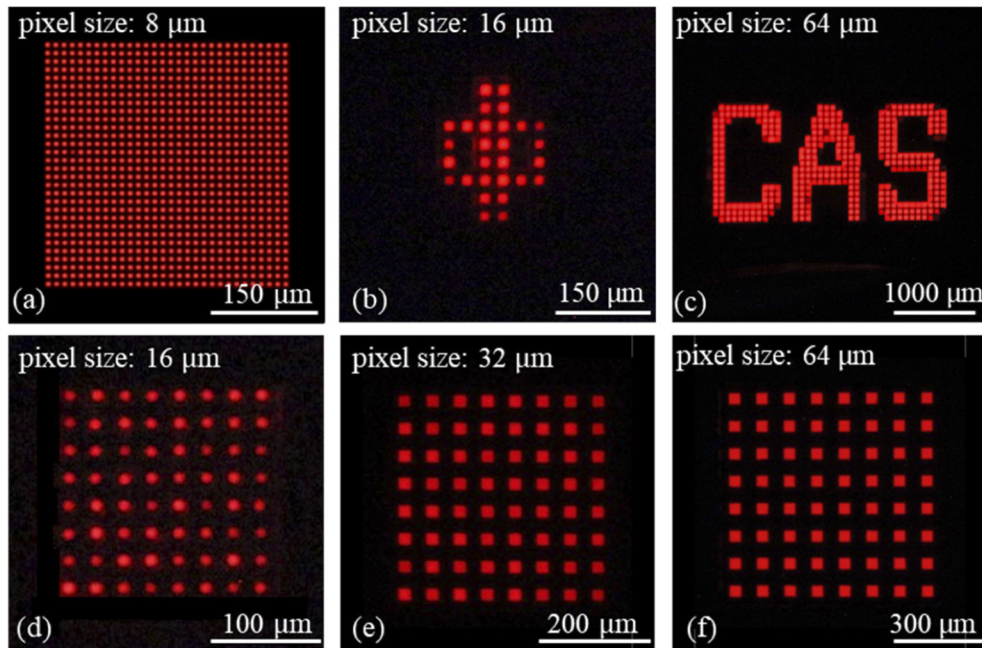


Fig. 4. Electroluminescence of micro-LED arrays with different pixel sizes (a) 2000 PPI micro-LED array with a pixel size of 8 μm . (b) A 16 μm micro-LED array with a symmetrical pattern. (c) A 64 μm micro-LED array with the word 'CAS'. Arrays of 8 rows and 8 columns with (d) 16 μm micro-LED array, (e) 32 μm micro-LED array, (f) 64 μm micro-LED.

Fig. S2 (e) and Fig. S2 (f). At a varied current density from 20 to 420 A/cm^2 the peak position of AlGaInP micro-LED on GaAs shifts from 627.76 nm to 636.41 nm ($\Delta\lambda = 8.65$ nm), which is larger than AlGaInP micro-LED on silicon ($\Delta\lambda = 2.43$ nm). The small change in the peak wavelength demonstrated that the bonding metal and silicon substrate have outstanding heat dissipation performance, hence, the silicon-based AlGaInP red micro-LED array has excellent peak wavelength stability. Furthermore, the FWHM increased from 17.5 nm at 20 A/cm^2 to 20.4 nm at 420 A/cm^2 . The small change in the FWHM of 2.9 nm indicates process uniformity and the good heat dissipation ability of the silicon-based AlGaInP red micro-LED array.

Table 1 lists the CIE 1931 coordinates of an 8 μm silicon-based AlGaInP red Micro-LED array for injection current densities in the range 40–420 A/cm^2 . The micro-LED array has coordinates of (0.6806, 0.3192) at injection current densities of 40 A/cm^2 . When current density increased from 40 to 420 A/cm^2 , the coordinates (x, y) in Table 1 shifted from (0.6806, 0.3192) to (0.6871, 0.3127), Figs. 5(c) and 5(d) show this change on the color space chromaticity diagram. Here, the shift in the coordinate's locus (red arrow in the inset of Fig. 5(d)) remains below the NTSC red. The color difference of the micro-LED array Δx and Δy was calculated as 0.0065 and 0.0065, respectively, indicating minimal color deviation over a large measured current density range. The deep red emission, with a CIE_y lower than the standard red of the NTSC, suggests the possibility to realize a large color gamut using silicon-based AlGaInP red micro-LED chips in full-color micro-LED displays.

The electrical performance and brightness of the 2000 PPI arrays were then measured. The LIV curve is shown in Fig. 6(a), the external quantum efficiencies (EQE) and brightness curves are shown in Fig. 6(b). In Fig. 6(a), it can be seen when the injected current was 10 mA, the typical value of the 2000 PPI array was 2.2 V. In Fig. 6(b), the light output power increases with the injection current and reaches 1.15 mW at 172.8 mA. It shows that the 2000 PPI array

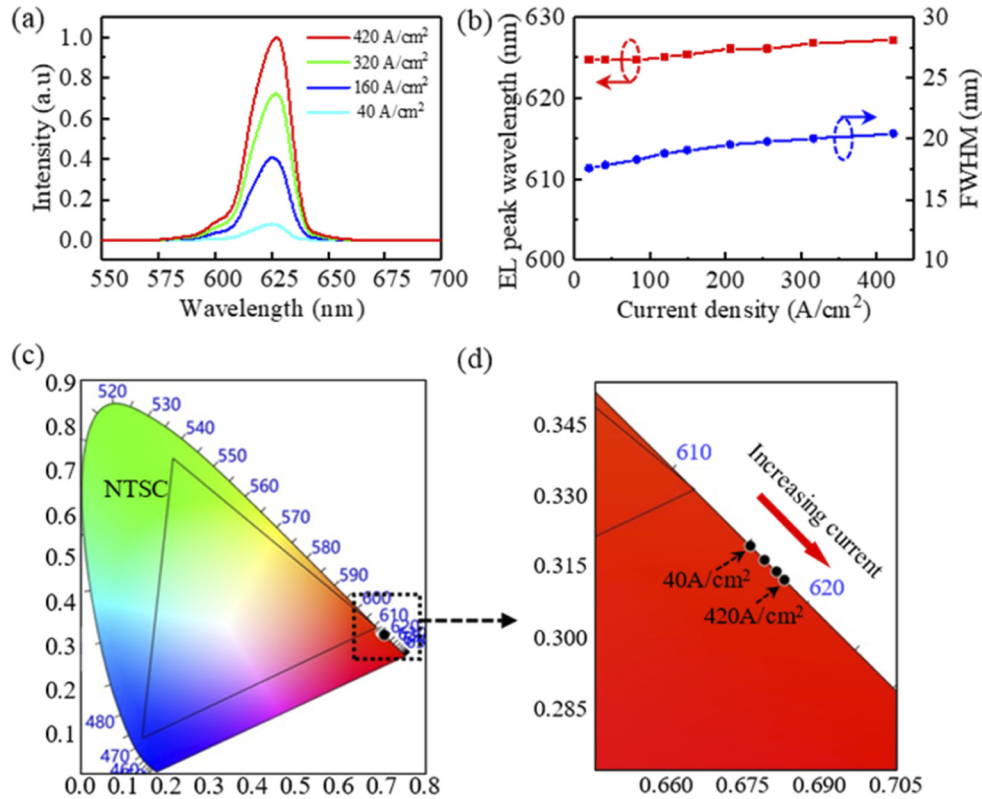


Fig. 5. (a) EL spectra of a micro-LED array at different current densities from 40 to 420 A/cm². (b) Spectral peak wavelength and full width at half maximum (FWHM) as a function of the injection current density for the micro-LED array. (c) CIE 1931 chromaticity diagram of the micro-LED array. (d) Magnified view of the CIE 1931 chromaticity diagram of the micro-LED array under different current densities, the inset red arrow shows the shift of the coordinate's locus with varying current density.

Table 1. CIE 1931 coordinates of an 8 μm micro-LED array under different injection current densities

Current density (A/cm ²)	CIE (x, y)
40	(0.6806, 0.3192)
120	(0.6833, 0.3165)
256	(0.6856, 0.3143)
420	(0.6871, 0.3127)

has stable electrical and optical performance. Figure 6(b) also shows the EQE of the 2000 PPI micro-LED array. The EQE of red micro-LED array can be described by:

$$\text{EQE} = \frac{P}{\frac{1}{I} \times \frac{P}{h\nu}} = \frac{P\lambda}{I} \times \frac{e}{hc} = \frac{P\lambda}{1240I}, \quad (1)$$

where P is the light output power of the micro-LED array, λ is the emission wavelength, I is the injected current, e is the elementary charge, h is the Planck constant, c is the speed of light, and ν is the frequency of the light. It also can be seen from the EQE curve in Fig. 6(b) that the peak EQE of the 2000 PPI array was 0.41%. In addition, the brightness of the 2000 PPI micro-LED

array is shown in Fig. 6(b), the brightness increases with the increase of current density and reaches 751 cd/m^2 at 184 A/cm^2 . The results show that the 2000 PPI array has not only high resolution but also high brightness.

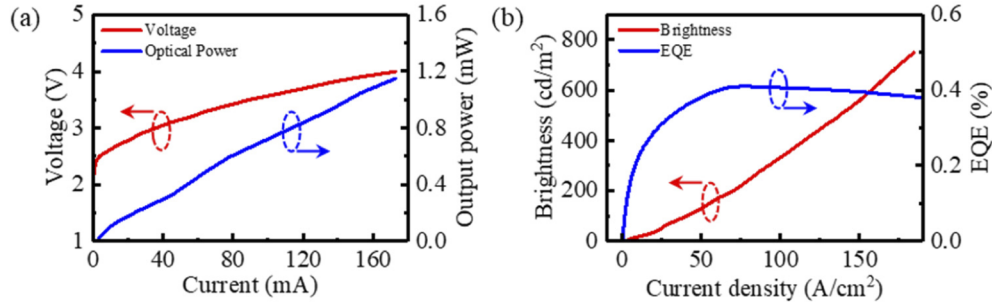


Fig. 6. (a) LIV curve of the 2000 PPI micro-LED array. (b) The EQE and brightness curves of the 2000 PPI micro-LED array.

The EL spectral and brightness of the prepared micro-LED arrays with three different sizes were then studied. Figure 7(a) shows the EL spectra of the micro-LED arrays with different pixel sizes of $64 \mu\text{m}$, $32 \mu\text{m}$ and $16 \mu\text{m}$ at a current density of 120 A/cm^2 . The EL spectrum of the micro-LED arrays increases with pixel size from $16 \mu\text{m}$ to $64 \mu\text{m}$. And, the peak wavelength for micro-LED arrays with pixel sizes of 64 , 32 , and $16 \mu\text{m}$ were 626.40 nm , 625.71 nm , and 623.67 nm , respectively. Different sizes of arrays have different heat dissipation performances, which leads to a different but slight shift of the peak wavelength. It indicates that the peak wavelength of micro-LED arrays fabricated by this method is less dependent on size. Figure 7(b) shows the brightness results of micro-LED arrays with different pixel sizes of $64 \mu\text{m}$, $32 \mu\text{m}$ and $16 \mu\text{m}$. It can be seen from Fig. 7(b) that the brightness of all arrays increases with current density. When the injected current density was 45 A/cm^2 , the typical values of the brightness for the three arrays with pixel sizes of 64 , 32 , and $16 \mu\text{m}$ were 249.71 cd/m^2 , 63.28 cd/m^2 , and 3.50 cd/m^2 , respectively.

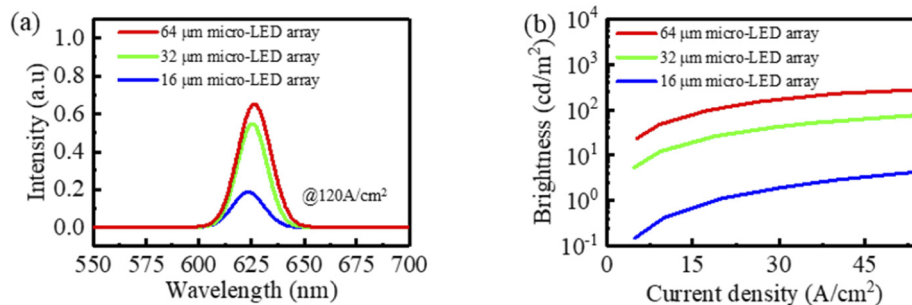


Fig. 7. (a) The EL spectra of the micro-LED arrays with different pixel sizes of $64 \mu\text{m}$, $32 \mu\text{m}$, and $16 \mu\text{m}$ at a current density of 120 A/cm^2 . (b) The brightness of the micro-LED arrays with different pixel sizes of $64 \mu\text{m}$, $32 \mu\text{m}$, and $16 \mu\text{m}$ at different current densities.

The electrical and light output characteristics of the prepared micro-LED arrays with three different sizes were then measured. As shown in Fig. 8(a), at a reverse bias voltage of -5 V , the measured reverse leakage currents for the three micro-LED arrays with pixel sizes of 64 , 32 , and $16 \mu\text{m}$ were 1.61×10^{-10} , 9.06×10^{-10} , and $1.04 \times 10^{-8} \text{ A}$, respectively, these values being far lower than that of an LED (10^{-7} A) fabricated on a CIC substrate in a previous report [28]. This result shows that silicon-based AlGaInP red micro-LED arrays fabricated via this method

have a lower reverse leakage current owing to the use of a lower-damage ICP etching recipe and high-performance polyimide. It was also observed that micro-LED arrays with smaller pixel sizes suffered more reverse leakage current, which can be attributed to more lattice defects, dangling gallium bonds, and N vacancies introduced during ICP etching [21]. The forward I-V characteristic results are shown in Fig. 8(b); when the injected current was 10 mA, the typical values of the forward voltage for the three arrays with pixel sizes of 64, 32, and 16 μm were 1.82, 2.32, and 2.51 V respectively. The three micro-LED arrays could support a large current density, which also demonstrates that the silicon-based AlGaInP red Micro-LED arrays have excellent electrical characteristics.

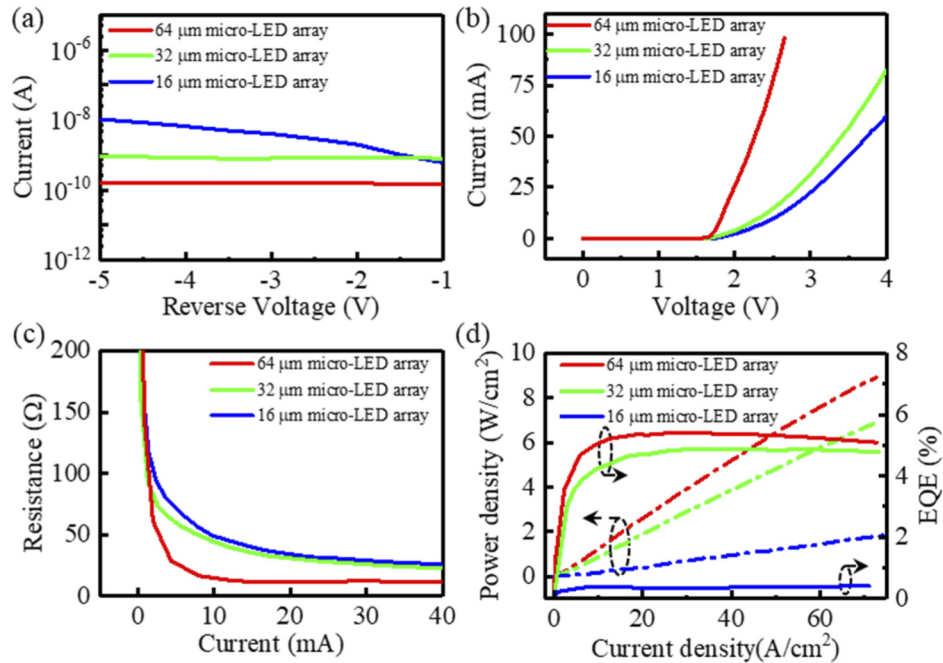


Fig. 8. Electrical and optical characteristic curves of the three micro-LED arrays with different pixel sizes. (a) Reverse I-V curves of the three micro-LED arrays. (b) Forward I-V curves of three micro-LED arrays. (c) Dynamic resistance curves of three micro-LED arrays. (d) Light output power density and EQE curves of the three micro-LED arrays.

In addition, the three micro-LED arrays had relatively large dynamic resistances at low current densities. However, the dynamic resistance gradually decreased and tended to stabilize under high current densities. This could mainly be attributed to the gradual decrease in parasitic resistance of the diode under higher current density [43]. Finally, the dynamic resistances of the 64, 32, and 16 μm micro-LED arrays at 40 mA were 11.13, 22.35, and 25.64 Ω , respectively. This shows that reducing the pixel size resulted in increased reverse leakage as well as an increase in the forward dynamic resistance of the arrays, resulting in decreasing forward current injection capability.

Subsequently, the light output power characteristics of micro-LED arrays with different pixel sizes were measured and the light output power dependence on the current was normalized by light-emission zone. As shown in Fig. 8(d), the light output power density for all the micro-LED arrays increased monotonically with increasing injection current density, and they could maintain high current density levels before breakdown. Further, the micro-LED arrays with bigger pixel sizes realized a larger light output power density under the same injection conditions. For the micro-LED array with a pixel size of 64 μm , the light output power density reached 8.95

W/cm^2 at a current density of $73 \text{ A}/\text{cm}^2$. For comparison, Wong et al. [32] reported a $100 \mu\text{m}$ AlGaInP micro-LED on GaAs substrate with a light output power density of only $\sim 0.3 \text{ W}/\text{cm}^2$ at the same current density, even after sidewall passivation via atomic layer deposition (ALD). The higher light output power density demonstrated in this work confirmed that high performance micro-LEDs can be realized by replacing the GaAs substrates and adding an Ag-based high-reflectance layer. In addition, the $32 \mu\text{m}$ micro-LED array had a light output power density of $6.94 \text{ W}/\text{cm}^2$ at $73 \text{ A}/\text{cm}^2$, which is a decrease of 22.46% compared with the $64 \mu\text{m}$ micro-LED array, while the $16 \mu\text{m}$ micro-LED array had a light output power density of $1.77 \text{ W}/\text{cm}^2$ at $73 \text{ A}/\text{cm}^2$, which is a decrease of 80.22% compared with the $64 \mu\text{m}$ micro-LED array. The decreasing light output power density for the micro-LED arrays with a smaller pixel size can be attributed to two primary reasons. One is the larger leakage current in smaller micro-LED arrays, which reduces the light output power density; the other is that a smaller micro-LED size can lead to high Shockley-Read-Hall (SRH) non-radiative recombination at sidewall sites, which becomes more significant because of the higher surface-to-volume ratio [44].

Figure 8(d) also shows the EQEs of the three micro-LED arrays. The EQEs of all the micro-LED arrays also show size dependencies, as observed in Fig. 8(d); a bigger pixel size has a higher EQE, and the peak EQEs for micro-LED arrays with pixel sizes of 64, 32, and $16 \mu\text{m}$ are 5.42%, 4.88% and 0.42%, respectively. It is worth noting that the EQE of the $16 \mu\text{m}$ micro-LED array is only one-tenth of that of the $32 \mu\text{m}$ micro-LED array. This can be attributed to a degradation of the electrical characteristics in the $16 \mu\text{m}$ micro-LED array that leads to a larger leakage current, as mentioned above. This is because a smaller pixel size would have a more pronounced sidewall effect, which leads to increased non-radiative recombination at the sidewall and a resulting decrease in the EQE [45].

4. Conclusion

In this work, the fabrication of a silicon-based AlGaInP red micro-LED array was carried out via wafer bonding and epilayer lift off, and the resulting 2000 PPI micro-LED array had stable spectral characteristics and a wide potential color gamut. Only a small 2.43 nm red shift of the peak wavelength was observed as the injection current density was increased from 20 to $420 \text{ A}/\text{cm}^2$, which can be attributed to the excellent conductivity of silicon and high reliability of the In-Ag bonding. The deep red emission with CIE coordinates of (0.6871, 0.3127) at $420 \text{ A}/\text{cm}^2$ indicates that the fabricated micro-LED array have a large potential color gamut. Additionally, the optical and electrical characteristics of the arrays were heavily dependent on the pixel size; the $64 \mu\text{m}$ micro-LED array had a smaller reverse leakage current and better forward electrical properties. For a current density of $73 \text{ A}/\text{cm}^2$, the light output power density of the $64 \mu\text{m}$ micro-LED array was $8.95 \text{ W}/\text{cm}^2$, which is 1.29 and 5.06 times that of the 32 and $16 \mu\text{m}$ micro-LED arrays, respectively. Additionally, as the pixel size decreased, the peak EQE of the device dropped significantly. The peak EQE of the $64 \mu\text{m}$ micro-LED array device was 5.42%, whereas it was 4.88% for the $32 \mu\text{m}$ micro-LED array, 0.42% for the $16 \mu\text{m}$ micro-LED array, and 0.41% for the $8 \mu\text{m}$ micro-LED array. In summary, the high-performance, high-resolution silicon-based AlGaInP micro-LED arrays fabricated in this work can serve as a viable red chip manufacturing template for application in full-color micro-LED displays.

Funding. National Key Research and Development Program of China (2018YFB1801901, 2018YFB1801902, 2019YFB2006000); National Natural Science Foundation of China (62004195); Jilin Scientific and Technological Development Program (20180201057YY, 20190302062GX, 20200401056GX).

Disclosures. The authors declare no conflicts of interest.

Data availability. Data underlying the results presented in this paper are not publicly available at this time but may be obtained from the authors upon reasonable request.

Supplemental document. See Supplement 1 for supporting content.

References

1. L. Zhang, F. Ou, W. C. Chong, Y. Chen, and Q. Li, "Wafer-scale monolithic hybrid integration of Si-based IC and III-V epi-layers-A mass manufacturable approach for active matrix micro-LED micro-displays," *J. Soc. Inf. Disp.* **26**(3), 137–145 (2018).
2. Y. Li, J. Tao, Y. Zhao, J. Wang, J. Lv, Y. Qin, J. Liang, and W. Wang, "48 (48 pixelated addressable full-color micro display based on flip-chip micro LEDs)," *Appl. Opt.* **58**(31), 8383–8389 (2019).
3. D. M. Geum, S. K. Kim, C. M. Kang, S. H. Moon, J. Kyhm, J. Han, D. S. Lee, and S. Kim, "Strategy toward the fabrication of ultrahigh-resolution micro-LED displays by bonding-interface-engineered vertical stacking and surface passivation," *Nanoscale* **11**(48), 23139–23148 (2019).
4. C. A. Bower, M. A. Meitl, B. Raymond, E. Radauscher, R. Cok, S. Bonafede, D. Gomez, T. Moore, C. Prevatte, B. Fisher, R. Rotzoll, G. A. Melnik, A. Fecioru, and A. J. Trindade, "Emissive displays with transfer-printed assemblies of $8\ \mu\text{m} \times 15\ \mu\text{m}$ inorganic light-emitting diodes," *Photonics Res.* **5**(2), A23–A30 (2017).
5. E. Xie, X. He, M. S. Islim, A. A. Purwita, J. J. D. McKendry, E. Gu, H. Haas, and M. D. Dawson, "High-Speed Visible Light Communication Based on a III-Nitride Series-Biased Micro-LED Array," *J. Lightwave Technol.* **37**(4), 1180–1186 (2019).
6. T. Pulli, T. Dönsberg, T. Poikonen, F. Manoocheri, P. Kärhä, and E. Ikonen, "Advantages of white LED lamps and new detector technology in photometry," *Light: Sci. Appl.* **4**(9), e332 (2015).
7. M. S. Islim, R. X. Ferreira, X. He, E. Xie, S. Videv, S. Viola, S. Watson, N. Bamiedakis, R. V. Penty, I. H. White, A. E. Kelly, E. Gu, H. Haas, and M. D. Dawson, "Towards 10 Gb/s orthogonal frequency division multiplexing-based visible light communication using a GaN violet micro-LED," *Photonics Res.* **5**(2), A35–A43 (2017).
8. J. F. C. Carreira, E. Xie, R. Bian, C. Chen, J. J. D. McKendry, B. Guilhabert, H. Haas, E. Gu, and M. D. Dawson, "On-chip GaN-based dual-color micro-LED arrays and their application in visible light communication," *Opt. Express* **27**(20), A1517–A1528 (2019).
9. X. Li, L. Wu, Z. Liu, B. Hussain, W. C. Chong, K. M. Lau, and C. P. Yue, "Design and Characterization of Active Matrix LED Microdisplays With Embedded Visible Light Communication Transmitter," *J. Lightwave Technol.* **34**(14), 3449–3457 (2016).
10. Z. Wei, S. Zhang, S. Mao, L. Wang, L. Zhang, C.-J. Chen, M.-C. Wu, Y. Dong, L. Wang, Y. Luo, and H. Y. Fu, "Full-duplex high-speed indoor optical wireless communication system based on a micro-LED and VCSEL array," *Opt. Express* **29**(3), 3891–3903 (2021).
11. Z. Ma, H. Cao, S. Lin, X. Li, X. Xi, J. Li, and L. Zhao, "Optical and frequency degradation behavior of GaN-based micro-LEDs for visible light communication," *Opt. Express* **28**(9), 12795–12804 (2020).
12. K. Kim, M. Voroslakos, J. P. Seymour, K. D. Wise, G. Buzsaki, and E. Yoon, "Artifact-free and high-temporal-resolution in vivo opto-electrophysiology with microLED optoelectrodes," *Nat. Commun.* **11**(1), 2063 (2020).
13. B. Ji, Z. Guo, M. Wang, B. Yang, X. Wang, W. Li, and J. Liu, "Flexible polyimide-based hybrid opto-electric neural interface with 16 channels of micro-LEDs and electrodes," *Microsyst. Nanoeng.* **4**(1), 27–38 (2018).
14. A. Adamantidis, S. Arber, J. S. Bains, E. Bamberg, A. Bonci, G. Buzsáki, J. A. Cardin, R. M. Costa, Y. Dan, Y. Goda, A. M. Graybiel, M. Häusser, P. Hegemann, J. R. Huguenard, T. R. Insel, P. H. Janak, D. Johnston, S. A. Josselyn, C. Koch, A. C. Kreitzer, C. Lüscher, R. C. Malenka, G. Miesenböck, G. Nagel, B. Roska, M. J. Schnitzer, K. V. Shenoy, I. Soltesz, S. M. Sternson, R. W. Tsien, R. Y. Tsien, G. G. Turrigiano, K. M. Tye, and R. I. Wilson, "Optogenetics: 10 years after Chr2 in neurons—views from the community," *Nat. Neurosci.* **18**(9), 1202–1212 (2015).
15. N. McAlinden, D. Massoubre, E. Richardson, E. Gu, S. Sakata, M. D. Dawson, and K. Mathieson, "Thermal and optical characterization of micro-LED probes for in vivo optogenetic neural stimulation," *Opt. Lett.* **38**(6), 992–994 (2013).
16. Y. Wu, J. Ma, P. Su, L. Zhang, and B. Xia, "Full-Color Realization of Micro-LED Displays," *Nanomaterials* **10**(12), 2482 (2020).
17. Z. Liu, C. H. Lin, B. R. Hyun, C. W. Sher, Z. Lv, B. Luo, F. Jiang, T. Wu, C. H. Ho, H. C. Kuo, and J. H. He, "Micro-light-emitting diodes with quantum dots in display technology," *Light: Sci. Appl.* **9**(1), 83–106 (2020).
18. Y. Huang, E. L. Hsiang, M. Y. Deng, and S. T. Wu, "Mini-LED, Micro-LED and OLED displays: present status and future perspectives," *Light: Sci. Appl.* **9**(1), 105–121 (2020).
19. J. H. Oh, S. J. Yang, and Y. R. Do, "Healthy, Natural, Efficient and Tunable Lighting: Four-Package White LEDs for Optimizing the Circadian Effect, Color Quality and Vision Performance," *Light: Sci. Appl.* **3**(2), e141 (2014).
20. G. Lozano, S. R. Rodriguez, M. A. Verschuuren, J. G. R. J. L. Science, and Applications, "Metallic nanostructures for efficient LED lighting," *Light: Sci. Appl.* **5**(6), e16080 (2016).
21. F. Xu, Y. Tan, Z. Xie, and B. Zhang, "Implantation energy- and size-dependent light output of enhanced-efficiency micro-LED arrays fabricated by ion implantation," *Opt. Express* **29**(5), 7757–7766 (2021).
22. L. Qi, X. Zhang, W. C. Chong, P. Li, and K. M. Lau, "848 ppi high-brightness active-matrix micro-LED micro-display using GaN-on-Si epi-wafers towards mass production," *Opt. Express* **29**(7), 10580–10591 (2021).
23. J. Park, J. H. Choi, K. Kong, J. H. Han, J. H. Park, N. Kim, E. Lee, D. Kim, J. Kim, D. Chung, S. Jun, M. Kim, E. Yoon, J. Shin, and S. Hwang, "Electrically driven mid-submicrometre pixelation of InGaN micro-light-emitting diode displays for augmented-reality glasses," *Nat. Photonics* **15**, 1–7 (2021).
24. H. X. Jiang and J. Y. Lin, "Nitride micro-LEDs and beyond—a decade progress review," *Opt. Express* **21**(S3), A475–484 (2013).

25. C. J. Chen, H. C. Chen, J. H. Liao, C. J. Yu, and M. C. Wu, "Fabrication and Characterization of Active-Matrix 960×540 Blue GaN-Based Micro-LED Display," *IEEE J. Quantum Elect.* **55**(1), 1–8 (2019).
26. S. Zhang, J. Zhang, J. Gao, X. Wang, C. Zheng, M. Zhang, X. Wu, L. Xu, J. Ding, Z. Quan, and F. Jiang, "Efficient emission of InGaN-based light-emitting diodes: toward orange and red," *Photonics Res.* **8**(11), 1671–1675 (2020).
27. X. Tang, L. Han, Z. Ma, Z. Deng, Y. Jiang, W. Wang, H. Chen, C. Du, and H. Jia, "Enhanced light extraction from AlGaInP-based red light-emitting diodes with photonic crystals," *Opt. Express* **29**(4), 5993–5999 (2021).
28. R. H. Horng, S. Sinha, C. P. Lee, H. A. Feng, C. Y. Chung, and C. W. Tu, "Composite metal substrate for thin film AlGaInP LED applications," *Opt. Express* **27**(8), A397–A403 (2019).
29. X. Bao, J. Liang, Z. Liang, W. Wang, C. Tian, Y. Qin, and J. Lü, "Design and fabrication of AlGaInP-based micro-light-emitting-diode array devices," *Opt. Laser Technol.* **78**, 34–41 (2016).
30. J. T. Oh, S. Y. Lee, Y. T. Moon, J. H. Moon, S. Park, K. Y. Hong, K. Y. Song, C. Oh, J. I. Shim, H. H. Jeong, J. O. Song, H. Amano, and T. Y. Seong, "Light output performance of red AlGaInP-based light emitting diodes with different chip geometries and structures," *Opt. Express* **26**(9), 11194–11200 (2018).
31. T. Gessmann and E. F. Schubert, "High-efficiency AlGaInP light-emitting diodes for solid-state lighting applications," *J. Appl. Phys.* **95**(5), 2203–2216 (2004).
32. M. S. Wong, J. A. Kearns, C. Lee, J. M. Smith, C. Lynsky, G. Lheureux, H. Choi, J. Kim, C. Kim, S. Nakamura, J. S. Speck, and S. P. DenBaars, "Improved performance of AlGaInP red micro-light-emitting diodes with sidewall treatments," *Opt. Express* **28**(4), 5787–5793 (2020).
33. S. Sinha, H.-A. Feng, C.-Y. Chung, C.-W. Tu, and R.-H. Horng, "Comparison of Properties of Thin Film AlGaInP LEDs with Composite Metal and Si Substrates," *ECS J. Solid State Sci. Technol.* **9**(1), 015015 (2020).
34. H. H. Park, X. Zhang, Y. Cho, D. W. Kim, J. Kim, K. W. Lee, J. Choi, H. K. Lee, S. H. Jung, E. J. Her, C. H. Kim, A. Y. Moon, C. S. Shin, H. B. Shin, H. K. Sung, K. H. Park, H. H. Park, H. J. Kim, and H. K. Kang, "Wafer-scale surface roughening for enhanced light extraction of high power AlGaInP-based light-emitting diodes," *Opt. Express* **22**(S3), A723–734 (2014).
35. J. F. C. Carreira, E. Xie, R. Bian, J. Herrnsdorf, H. Haas, E. Gu, M. J. Strain, and M. D. Dawson, "Gigabit per second visible light communication based on AlGaInP red micro-LED micro-transfer printed onto diamond and glass," *Opt. Express* **28**(8), 12149–12156 (2020).
36. F. L. Wu, S. L. Ou, Y. C. Kao, C. L. Chen, M. C. Tseng, F. C. Lu, M. T. Lin, and R. H. Horng, "Thin-film vertical-type AlGaInP LEDs fabricated by epitaxial lift-off process via the patterned design of Cu substrate," *Opt. Express* **23**(14), 18156–18165 (2015).
37. R. H. Horng, H. Y. Chien, K. Y. Chen, W. Y. Tseng, Y. T. Tsai, and F. G. Tarntair, "Development and Fabrication of AlGaInP-Based Flip-Chip Micro-LEDs," *IEEE J. Electron Devices Soc.* **6**, 475–479 (2018).
38. S. Zhou, H. Xu, B. Tang, Y. Liu, H. Wan, and J. Miao, "High-power and reliable GaN-based vertical light-emitting diodes on 4-inch silicon substrate," *Opt. Express* **27**(20), A1506–A1516 (2019).
39. S. Zhou, X. Liu, H. Yan, Z. Chen, Y. Liu, and S. Liu, "Highly efficient GaN-based high-power flip-chip light-emitting diodes," *Opt. Express* **27**(12), A669–A692 (2019).
40. S. Zhou, X. Liu, Y. Gao, Y. Liu, M. Liu, Z. Liu, C. Gui, and S. Liu, "Numerical and experimental investigation of GaN-based flip-chip light-emitting diodes with highly reflective Ag/TiW and ITO/DBR Ohmic contacts," *Opt. Express* **25**(22), 26615–26627 (2017).
41. Q. Zhao, J. Miao, S. Zhou, C. Gui, B. Tang, M. Liu, H. Wan, and J. Hu, "High-Power GaN-Based Vertical Light-Emitting Diodes on 4-Inch Silicon Substrate," *Nanomaterials* **9**(8), 1178 (2019).
42. M. A. Khan, H. Chen, J. Qu, P. W. Trimby, S. Moody, Y. Yao, S. P. Ringer, and R. Zheng, "Insights into the Silver Reflection Layer of a Vertical LED for Light Emission Optimization," *ACS Appl. Mater. Interfaces* **9**(28), 24259–24272 (2017).
43. W. Tian and J. Li, "Size-dependent optical-electrical characteristics of blue GaN/InGaN micro-light-emitting diodes," *Appl. Opt.* **59**(29), 9225–9232 (2020).
44. J. Kou, C. C. Shen, H. Shao, J. Che, and H. C. J. O. E. Kuo, "Impact of the surface recombination on InGaN/GaN-based blue micro-light emitting diodes," *Opt. Express* **27**(12), A643–A653 (2019).
45. B. O. Jung, W. Lee, J. Kim, M. Choi, and M. J. J. S. R. Kim, "Enhancement in external quantum efficiency of AlGaInP red μ -LED using chemical solution treatment process," *Sci. Rep.* **11**(1), 4535–4544 (2021).